Check for updates

Interfacial chemistry regulation by orbital hybridization for superior kinetics of hard carbon in an ester-based electrolyte

Lu Liu,†[a] Jianhua Zhu, †[a] Guohui Chen, [a] Zhuosen Wang, [a] Liu Wang,[a] Chengkun Guo,[a] Yunfeng Chao, *[a] Xinwei Cui *[a] and Caiyun Wang [b]

Hard carbon is the most commercially viable anode material for sodium-ion batteries (SIBs), yet its application in ester-based electrolytes is hindered by sluggish interfacial ion diffusion and limited sodium nucleation kinetics. After comprehensive evaluation, an interfacial chemistry regulation strategy was proposed based on orbital hybridization between bismuth and electrolyte ions, which was realized through the introduction of ammonium bismuth citrate. The surface bismuth particles regulate the formation of a NaF-rich SEI through improved anion affinity. In collaboration with the *in situ* generated highly ion-conductive Na_3N, a thin, compact and homogeneous SEI was constructed to enable fast and stable interfacial Na^+ migration kinetics. Moreover, the Bi atoms can diffuse into the hard carbon structures, expanding the carbon interlayers to facilitate ion diffusion and intercalation as well as enhancing the sodiophilicity in closed pores to lower the nucleation barrier. Benefiting from these merits, the resulting T2-BiN exhibits superior sodium-storage kinetics with outstanding rate capability (185.6 mA h g^{-1} at 0.5 A g^{-1}) and long-term cycling stability (84.4% after 400 cycles at 0.5 A g^{-1}) in the ester-based electrolyte. Even the practical full cell showed no capacity decay over 400 cycles at 2C. This work provides a simple and effective interfacial modification strategy, offering new insights into the advancement of hard carbon anodes for high-performance SIBs.

Introduction

Due to their abundant resources, low cost, and moderate energy density, sodium-ion batteries (SIBs) have emerged as a cost-effective alternative or supplement to conventional lithium-ion battery systems.[1] Among various anode materials, hard carbon is considered one of the most promising candidates for SIBs owing to its high reversible capacity, low working potential, scalability, and low raw material cost.[2,3] Extensive progress has been made in understanding the sodium storage mechanisms of hard carbon, especially regarding the role of pore structure, which has inspired a variety of structural engineering strategies to enhance capacity.[4–6] However, in ester-based electrolytes—which offer greater commercial viability—the rate performance of hard carbon is still limited. Recent studies have identified the solid electrolyte interphase (SEI) formed between hard carbon anodes and the electrolyte as the key rate-limiting factor, particularly in processes involving desolvation and ion migration across the SEI.[7–9]

Ester-based electrolytes offer advantages such as low cost and excellent high-voltage stability, but their reduction products typically form thick and heterogeneous SEI layers (Fig. 1a(1)). During discharging, anions are repelled from the Helmholtz layer owing to the electric field and their poor adsorption on the anode surface.[10,11] Meanwhile, the decomposition of solvent molecules results in loose and inhomogeneous organic components, causing continued electrolyte decomposition, increased polarization, and capacity fading during cycling. Nitrogen-based inorganic species such as Li_3N and Na_3N exhibit superior ion conductivity, which provides a feasible way to improve the interfacial Na^+ transport of hard carbon.[12–15] However, solely introducing nitrogen-containing precursors or Na_3N is insufficient to effectively suppress the formation of organic components for uniform interfacial Na^+ transport (Fig. 1a(2)). Recent studies have highlighted the essential role of LiF or NaF in enhancing the homogeneity, mechanical strength, and stability of the SEI.[16–19] An ideal SEI enriched with both mechanically robust NaF and highly ion-conductive Na_3N (Fig. 1a(3)) is expected to be very thin, dense, and uniform, thereby enabling excellent interfacial ion migration kinetics. Among the various strategies proposed to modulate LiF or NaF formation, surface engineering offers advantages in eliminating the negative effects on electrolyte properties and cathode performance.[8,17] High anion-adsorption

[a]*Institute of Advanced Technology, Zhengzhou University, Zhengzhou 450052, P. R. China. E-mail: chaoyf@zzu.edu.cn; xinweic@zzu.edu.cn*

[b]*ARC Ctr. Excellence Electromat Sci., University of Wollongong, Innovation Campus, North Wollongong, NSW 2500, Australia*

† L. Liu and J. Zhu contributed equally to this work.
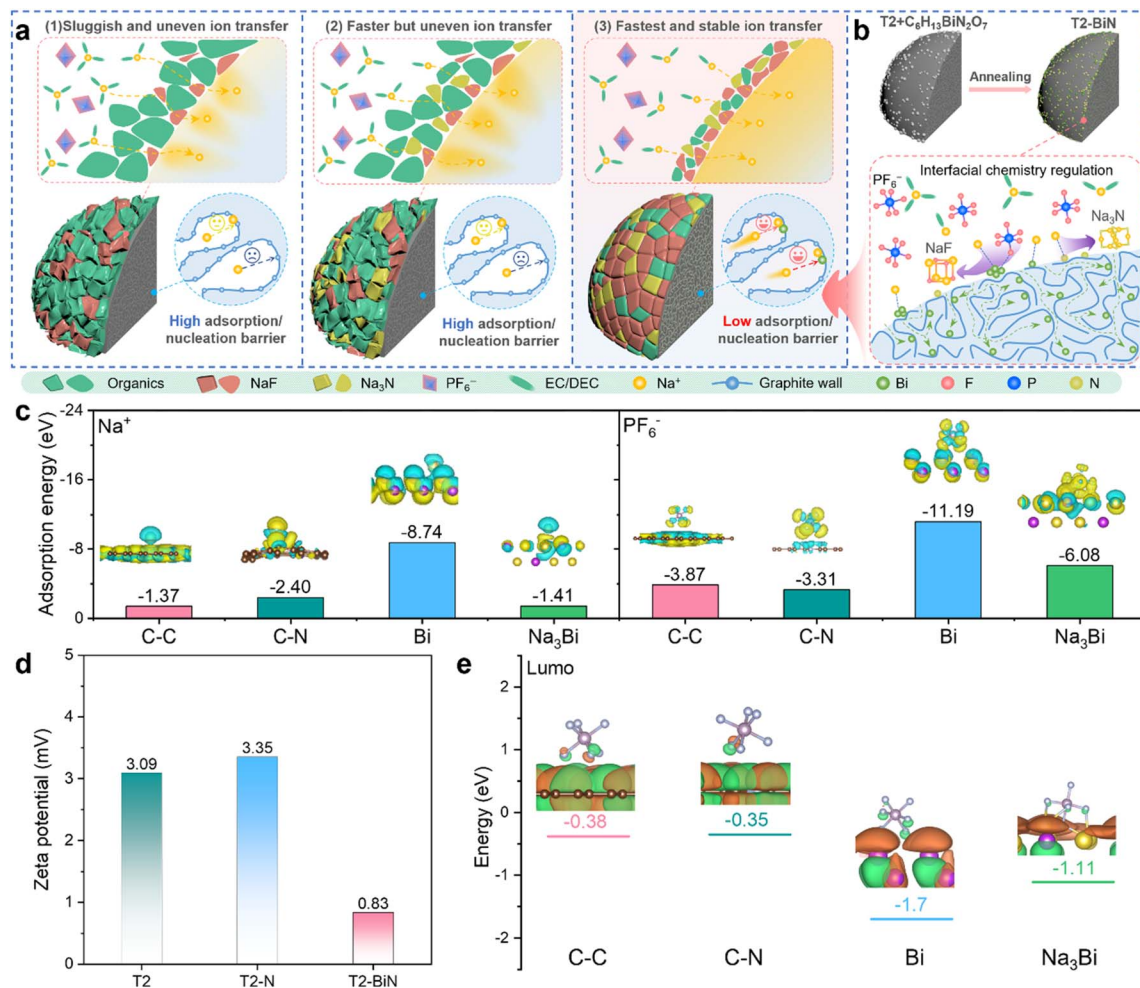
Fig. 1 Guidelines for an interfacial chemistry regulation strategy. (a) Effects of different interfacial structures on sodium-storage behaviors; (b) preparation of T2-BiN and its approach to implementing interfacial chemistry regulation; (c) adsorption energy of Na^+ and PF_6^- on the substrates of neat carbon (C–C), nitrogen-doped carbon (C–N), Bi metal and Na_3Bi; (d) zeta potential of original T2, T2-N and T2-BiN in ester electrolyte; (e) LUMO of PF_6^- on the substrates of C–C, C–N, Bi metal and Na_3Bi.

and an electron-rich surface have been identified as two critical factors for implementing surface engineering, which have not been fully resolved in hard carbon anodes.[7,17,20]

Beyond this, many recent reports have revealed the sodium storage process in hard carbon, involving Na^+ adsorption, nucleation, and pore-filling in closed pores.[2,21] As the starting point of pore-filling, the adsorption–filling process is critical for plateau capacity and rate performance, but is often overlooked.[1,22] This process is strongly influenced by both the pore size and surface characteristics of closed pores.[23,24] Sodium filling preferentially occurs in smaller closed pores, with a higher nucleation barrier observed in closed macropores.[25,26] It commonly results in relatively low sodium filling efficiency and pore utilization. Strategies such as the introduction of heteroatoms or functional groups have been proposed to activate the electrochemically inert closed pores for an improved Na filling rate and Na filing capacity.[24,27,28] Introducing metallic species can lower the surface energy and act as nucleation sites.[27,29] However, the Na^+ affinity of transition metals is poor

and incorporating them before carbonization often leads to over-graphitization and collapse of the pore structure.[30] To address these challenges, Bi can be an optimal choice to simultaneously modulate NaF formation and nucleation kinetics though orbital hybridization. The low melting point (271.3 °C) and small atomic radius (0.143 nm) of Bi enable efficient incorporation at relatively low temperatures, preventing negative impacts on the intrinsic structure of hard carbon. The hybridization between the active p orbital of Bi and the s orbital of Na^+ or F in PF_6^- endows Bi with a strong dual-ion affinity, thereby promising to regulate NaF formation in SEI as well as Na^+ nucleation in closed pores.[31]

Based on above concepts, commercially available hard carbon (T2) was modified using ammonium bismuth citrate as the precursor (Fig. 1b). After carbonization, a nitrogen-rich carbon matrix was formed on the hard carbon surface, which contributed to Na_3N generation during initial sodiation. Meanwhile, the surface Bi metal effectively mitigates anion depletion through strong PF_6^- adsorption. Its electron-rich

character further promotes anion decomposition to form a uniform NaF-rich SEI and inhibits continuous electrolyte degradation. Furthermore, Bi atoms diffused into the carbon interlayers to expand the interlayer spacing, promoting Na^+ diffusion and intercalation. The presence of Bi in closed pores also modulates the surface energy and Na^+ affinity for enhanced sodium nucleation behaviour. As a result, the modified T2-BiN anode demonstrated outstanding electrochemical performance in ester-based electrolytes: a high capacity of 320.2 mA h g^{-1} at 0.05 A g^{-1}, an excellent rate capability of 185.6 mA h g^{-1} at 0.5 A g^{-1}, and a high capacity retention of 84.4% after 400 cycles at 0.5 A g^{-1}. Even in full cells, it achieved a high energy density of 237.2 W h kg^{-1} with a retention of 98.8% after 400 cycles at 2C. These results clearly confirm the effectiveness of the proposed interfacial chemistry regulation strategy and its significance for the scalable production of hard carbon-based high-performance sodium-ion batteries.

Results and discussion

Simulation of the interfacial chemistry regulation

To evaluate the effectiveness of using Bi and N elements to engineer hard carbon, DFT calculations were first performed to evaluate the adsorption energies of Na^+ and PF_6^- on various substrates (Fig. 1c), including pristine carbon (C–C) and nitrogen-doped carbon (C–N). Given that low-melting-point Bi metal tends to form metallic clusters on the hard carbon surface and readily reacts with Na^+ to form Na_3Bi within the voltage range of 0.3–0.5 V, both Bi and Na_3Bi were included in the investigation. The results show that the pristine carbon substrate has adsorption energies of −1.37 eV for Na^+ and −3.87 eV for PF_6^-. After nitrogen doping, the adsorption energy for Na^+ increases to −2.40 eV, while that for PF_6^- slightly decreases to −3.31 eV. This suggests that while low-electronegativity N enhances Na^+ affinity, it cannot capture anions to regulate NaF formation. In contrast, metallic Bi exhibits strong dual-ion adsorption capabilities, with adsorption energies of −8.74 eV for Na^+ and −11.19 eV for PF_6^-. Even after sodiation, Na_3Bi still shows considerable adsorption energies of −1.51 eV for Na^+ and −6.08 eV for PF_6^-. This strong dual-ion affinity can be attributed to the orbital hybridization between Bi and Na^+ or F in PF_6^-.[31] The strong Na^+ adsorption can definitely promote sodium anchoring, nucleation, and pore-filling within the closed pores, while the high PF_6^- affinity is essential for mitigating anion depletion to modulate the SEI content.[31] Therefore, it can be concluded that this interfacial chemistry modulation is fundamentally established through orbital hybridizations. Bi atoms feature accessible 6p orbitals that can overlap with the filled F 2p orbitals in PF_6^- or the Na 3s orbitals, enabling robust dual-ion affinity that facilitates NaF formation in the SEI and Na nucleation in closed pores. In combination with the introduced N, this strategy leads to a NaF/Na_3N-rich SEI with a sodiophilic surface inside closed pores, thereby enhancing sodium storage in hard carbon anodes.

These findings are consistent with the zeta potential measurements (Fig. 1d). Specifically, the pristine T2 hard carbon exhibits a zeta potential of 3.09 mV in 1 M $NaPF_6$ EC/ DEC (1 : 1, v/v) electrolyte, indicating predominant adsorption of Na^+—likely due to surface oxygen-containing functional groups. After nitrogen doping (T2-N), the zeta potential increases slightly to 3.35 mV, confirming enhanced cation affinity. In contrast, the Bi/N co-modified sample (T2-BiN) exhibits a significantly reduced zeta potential of 0.83 mV, clearly demonstrating that Bi incorporation effectively anchors anions in the Helmholtz layer and lays the foundation for NaF formation in the SEI layer.[19,32] To further explore the potential for PF_6^- decomposition, the lowest unoccupied molecular orbital (LUMO) energy levels of PF_6^- on different substrates were calculated (Fig. 1e). The LUMO levels on pristine and N-doped carbon are relatively high, whereas the electron-rich Bi and Na_3Bi substrates lower the PF_6^- LUMO levels to −1.70 eV and −1.11 eV, respectively. The decreased PF_6^- LUMO favors its decomposition to generate NaF, which further demonstrates the essential role of Bi on regulating SEI formation.[33] Furthermore, DFT calculations were employed to reveal the Na^+ diffusion properties of different SEI components. The results reveal diffusion barriers of 0.666 eV for NaF, 0.013 eV for Na_3N and 0.196 eV for the potentially formed Na_3Bi (Fig. S1). It underscores the critical role of Na_3N in enhancing Na^+ transport through the SEI, whereas NaF mainly stabilizes the SEI by serving as a passivation layer against electrolyte decomposition.

Characterization of the engineered hard carbon

A comprehensive morphological and structural characterization study was conducted to reveal the forms of Bi and N in the T2-BiN sample. SEM images (Fig. S2, SI) show that both pristine T2 and T2-BiN retain irregular micron-sized polyhedral morphologies, with no significant changes observed after modification. Elemental mapping via SEM and TEM (Fig. S3) confirms the uniform distribution of C, O, N, and Bi across the hard carbon particles, indicating successful co-doping. Notably, partial aggregation of Bi was observed in the electron microscopy images and Bi mapping maps, suggesting the formation of surface Bi metal clusters. To further investigate the spatial distribution of N and Bi within the particles, cross-sectional analysis of T2-BiN electrodes was performed. As shown in Fig. S4, both elements are evenly distributed throughout the electrode thickness. Elemental mapping of the enlarged area (Fig. 2a) confirms the uniform distribution of C, O, N, and Bi within the hard carbon particles. Line-scan profiles across the cross-section (Fig. S5) further evidence the even distribution of N and Bi. HRTEM images (Fig. 2b and c) reveal that both T2 and T2-BiN exhibit short-range ordered and long-range disordered characteristics, along with abundant closed pores.[34] It is noteworthy that the carbon lattice of T2-BiN appears less ordered, with an expanded (002) interlayer spacing in the range of 0.382– 0.414 nm, larger than that of T2 (0.366–0.373 nm). This expanded interlayer results from the diffusion of molten Bi metal atoms within the carbon domains.[35,36] It also aligns with the slight low-angle shift of the (002) diffraction peak in the XRD pattern (Fig. 2d), which facilitates Na^+ diffusion and intercalation. Additionally, characteristic peaks of metallic Bi are present in the XRD pattern of T2-BiN, in agreement with the
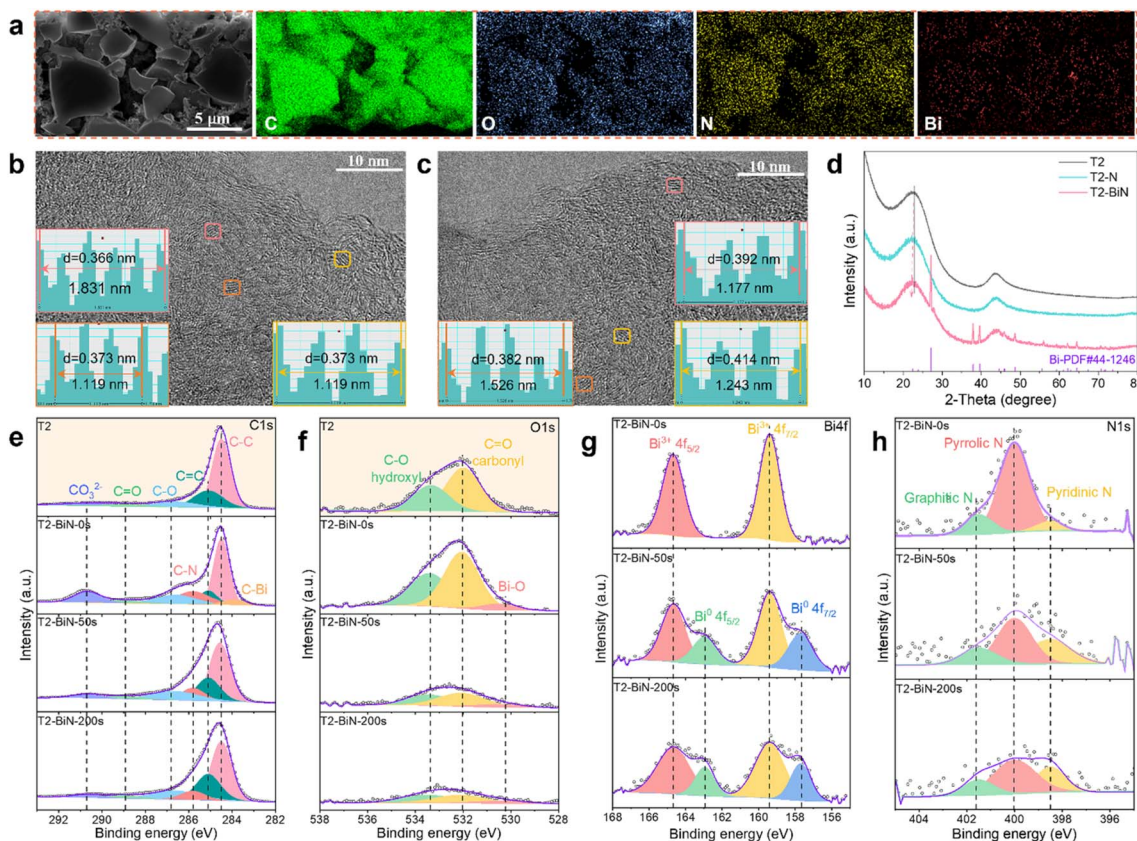
Fig. 2 Structural characterization of T2-BiN. (a) Cross-sectional SEM and the corresponding element mapping images of T2-BiN anode; HRTEM images of T2 (b) and T2-BiN (c); XRD (d) of T2, T2-N and T2-BiN; (e) XPS C 1s spectrum of T2 and depth-profiling C 1s spectra of T2-BiN; (f) O 1s XPS spectrum of T2 and depth-profiling C 1s spectra of T2-BiN; depth-profiling XPS Bi 4f (g) and N 1s (h) spectra of T2-BiN.

Bi clusters observed in SEM and TEM images. Fig. S6a shows the Raman spectra, with the A_{D1}/A_G ratio increasing from 1.29 for T2 to 1.35 for T2-N and 1.38 for T2-BiN. The change in A_{D1}/A_G reveals the formation of additional structural defects, primarily originating from the nitrogen-doped carbon layer generated by precursor decomposition.[37] Correspondingly, the BJH surface area, as determined by the N_2 adsorption–desorption measurements, increases from 7.44 to 10.41 m^2 g^{-1} (Fig. S6b). SAXS measurements (Fig. S7) of both T2 and T2-BiN exhibit a broad peak around 2 nm^{-1}, confirming the existence of closed pores in the carbon matrix. Fitting results indicate that the average diameters of the closed pores were 1.823 nm for T2 and 1.725 nm for T2-BiN. This suggests that Bi diffusion generates more small-sized closed pores, thereby reducing the overall average diameter. It can thus be concluded that a layer of defect-rich nitrogen-doped carbon is formed on the surface of hard carbon, while the generated metal Bi thermodynamically diffuses into the hard carbon, slightly increasing the interlayer spacings of the carbon layers.

XPS and depth-profiling XPS analyses were conducted to further examine chemical composition and bonding states. The C 1s XPS spectra (Fig. 2e) of both samples show peaks corresponding to C–C (284.5 eV), C=C (285.1 eV), C–O (286.8 eV), C=O (289.0 eV), and CO_3^{2-} (290.7 eV) bonds.[38] An additional C–N peak at 285.8 eV appears in the C 1s spectra of T2-BiN,

supporting the successful introduction of N. Besides, an intensified CO_3^{2-} peak and a new C–Bi peak at 283.9 eV were observed on the surface of T2-BiN, both of which are attributed to precursor decomposition. The O 1s XPS spectrum of T2 (Fig. 2f) exhibits two peaks at 532 eV and 533.4 eV, corresponding to carbonyl C=O and hydroxyl C–O, respectively.[39] T2-BiN possesses similar signals with an additional weak Bi–O peak. As the sputtering time increases from 0 s to 200 s, the overall O 1s intensity of T2-BiN significantly decreases without changes in bonding states. This can be attributed to the presence of more oxygen-containing functional groups on the surface. Fig. 2g presents the Bi 4f depth profile of T2-BiN. At an etching time of 0 s, the two peaks detected at 159.4 eV and 164.7 eV correspond to Bi^{3+} $4f_{7/2}$ and Bi^{3+} $4f_{5/2}$, likely due to surface oxidation. Following sputtering, metallic Bi peaks emerge at 157.7 eV and 162.9 eV, confirming the presence of metallic Bi within the carbon matrix. The N 1s XPS spectra of T2-BiN in Fig. 2h show pyridinic N (398.5 eV), pyrrolic N (400.0 eV), and graphitic N (401.6 eV), with pyrrolic N being dominant.[37] The progressive decrease in intensity with depth suggests that nitrogen is predominantly concentrated near the surface, facilitating the subsequent formation of Na_3N within the SEI during sodiation. All these structural features support the simultaneous incorporation of N and Bi on the hard carbon surface, as well as the diffusion of Bi into the interior structure,

which aligns well with the design strategy and lays a solid foundation for the interfacial chemistry regulation strategy.

Sodium-ion storage performance

T2-BiN samples prepared with varying amounts of precursor were first evaluated (Fig. S8). As the precursor content increased, a proportional rise in the A_{D1}/A_G ratio indicated the formation of more defect-rich carbon structures. Insufficient precursor resulted in limited performance improvement, with severe polarization still present. On the other hand, excessive precursor led to the formation of abundant defects, and the excess Bi may block the Na$^+$ diffusion pathways. Therefore, the sample prepared with 3 wt% ammonium bismuth citrate exhibited the best sodium storage performance and was selected as the optimal T2-BiN composition for subsequent studies. As shown in the rate performance (Fig. 3a), pristine T2 exhibits poor performance in ester-based electrolytes. Nitrogen doping (T2-N) significantly enhances the rate capability. However, considerable capacity fluctuation is still observed, likely due to the formation of an inhomogeneous SEI. In contrast, T2-BiN delivers both the highest and most stable capacities, reaching 321.6, 296.6, 272.0, 245.9, 185.6, and 110.4 mA h g^{-1} at current densities of 0.05, 0.1, 0.2, 0.3, 0.5, and 0.8 A g^{-1}, respectively. Upon returning to 0.1 A g^{-1}, the capacity recovered to 286.3 mA h g^{-1} and remained stable until the 100th cycle. In comparison, although T2 and T2-N can recover most of their initial capacity, they still exhibit capacity fluctuations in subsequent cycles. To be specific, the initial coulombic efficiency (ICE) was 67.5% for T2, 64.0% for T2-N, and 62.6% for T2-BiN (Fig. 3a). The slight reduction in ICE can be attributed to the formation of a nitrogen-doped carbon layer on the hard carbon surface.

The first three dQ/dV curves (Fig. 3b and S9) provide insight into the electrochemical reaction process. All samples display a weak peak at ~1.1 V during the first discharge, corresponding to Na$^+$ adsorption at surface defects. An irreversible board peak at around 0.4 V was also observed for T2, which can be assigned to the formation of SEI. The corresponding peaks for T2-N and T2-BiN are intensified owing to the formation of Na$_3$N. Additionally, T2-BiN exhibits two reversible reduction peaks in the
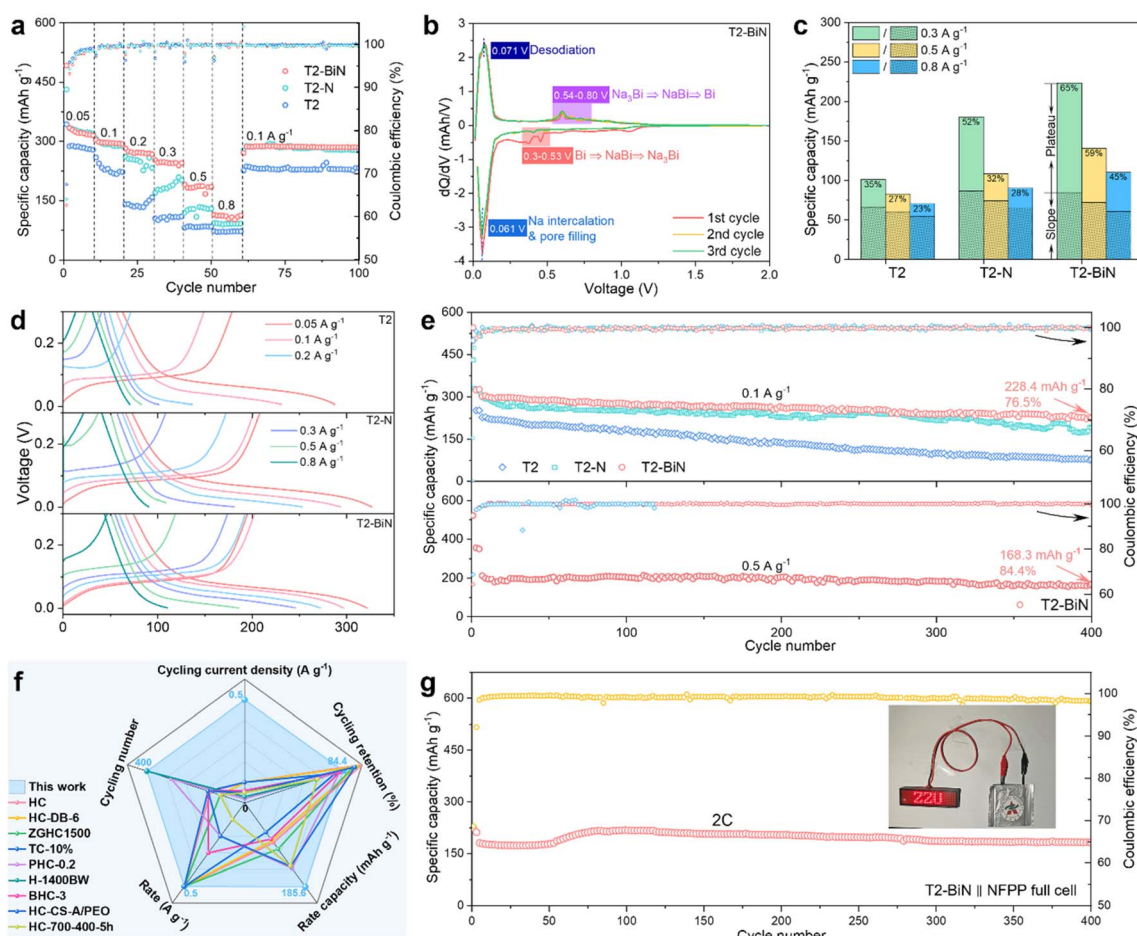

Fig. 3 Sodium-storage performance of T2-BiN. (a) Rate capability of T2, T2-N and T2-BiN anodes; (b) the first three dQ/dV profiles of T2-BiN; (c) comparison of slope and plateau capacities at different current densities; (d) charge–discharge curves of T2, T2-N and T2-BiN anodes at different current densities; (e) cycling performance at 0.1 A g^{-1} and 0.5 A g^{-1}; (f) comparison of rate and cycling performance between T2-BiN and other ester-based hard carbon anodes; (g) long-term cycling tests at 2C over 400 cycles with the Na$_4$Fe$_3$(PO$_4$)$_2$(P$_2$O$_7$) NFPP cathode coupled with the T2-BiN anode. The inset shows the pouch-type full-cell demo.

range of 0.3–0.53 V, with the corresponding reduction peaks between 0.54 and 0.8 V. They originate from the reversible reaction between Bi, NaBi and Na_3Bi.[40] As the discharge process progressed, all three electrodes exhibited sharp reduction peaks corresponding to the pore-filling of sodium ions. It should be noted that the redox peaks for T2-BiN are located at 0.061 V and 0.071 V, evidencing its highest nucleation potential and lower polarization. The measured nucleation overpotentials in Fig. S9c were 12.3 mV for T2 and 16.2 mV for T2-BiN, further supporting the reduced nucleation barriers of T2-BiN. Fig. 3c and S10 compare the capacity contributions from the slope and plateau regions at various current densities. T2-BiN shows a clear advantage at high rates. For instance, the plateau capacity of T2-BiN contributes a high ratio of 59% at 0.5 A g^{-1}, compared to only 27% for T2 and 32% for T2-N. These improvements are also clearly shown in the charge/discharge profiles (Fig. S11). The enlarged profiles (Fig. 3d) further show that T2-BiN exhibits the smallest polarization increase with rising current, confirming its fast and stable electrochemical kinetics.

The effectiveness of interfacial chemistry regulation was further validated through extended cycling tests. Following rate evaluation, the T2-BiN electrode demonstrated excellent cycling stability, maintaining a capacity of 256.9 mA h g^{-1} with a retention of 89.2% after 400 cycles (Fig. S12). Additional tests with freshly assembled electrodes (Fig. 3e) revealed that T2-BiN delivered 228.4 mA h g^{-1} with 76.5% retention over 400 cycles at 0.1 A g^{-1}, outperforming T2 (78.2 mA h g^{-1}, 34.5%) and T2-N (190.7 mA h g^{-1}, 61.6%). At higher current densities, T2-BiN continued to show outstanding cycling performance. It retained 168.3 mA h g^{-1} after 400 cycles at 0.5 A g^{-1} (84.4% retention), and 115.3 mA h g^{-1} after 2000 cycles at 0.8 A g^{-1} with 89.4% retention (Fig. S13). Even at a higher areal mass of 3.26 mg cm^{-2} (Fig. S14), the T2-BiN anode still demonstrated excellent cycling stability with a retention of 87.7% after 150 cycles at 0.1 A g^{-1}. The comparison between T2-BiN and recently reported ester-based hard carbon anodes (Fig. 3f) clearly evidences the superiority of this T2-BiN anode.[18,38,39,41–46] Besides, the T2-BiN and T2 anodes were tested in ether-based electrolytes (Fig. S15), where T2-BiN again showed improved rate and cycling performance, underscoring the universality of this approach. To demonstrate practical viability, $Na_4Fe_3(PO_4)_2P_2O_7$ (NFPP, Fig. S16) cathodes were selected to assembly the full cells. As shown in the inset of Fig. 3g, the T2-BiN∥NFPP pouch cell successfully powered an LED panel. The charge–discharge profiles (Fig. S17a) revealed voltage plateaus around 3.1 V. Based on the anode mass (Fig. S17b), the full cell delivers specific capacities of 267.7, 252.0, 224.0, 212.9, 189.7, and 149.4 mA h g^{-1} at 0.2C, 0.4C, 0.8C, 1.2C, 2C and 3.2C, respectively. Even over 400 cycles at 2C, the capacity remained at 181.9 mA h g^{-1} with 99.8% retention (Fig. 3g). Considering the total mass of both the anode and cathode, the energy density of the full cell reached 237.2 W h kg^{-1} at 0.2C and remained as high as 161.1 W h kg^{-1} over 400 cycles at 2C. Such excellent stability at high rates in ester electrolyte is rarely found in previous high-impact reports (Table S1), which solidly demonstrates the superior performance and practical potential of T2-BiN.

Evolution of electrochemical kinetics

To assess the effects of interfacial chemistry regulation, the evolution of electrochemical kinetics during cycling was thoroughly analysed. As shown in Fig. S18, the charge–discharge profiles of the three electrodes reveal distinct differences in long-term behaviour. The T2 electrode exhibits a pronounced decline in both the plateau region and overall capacity. While T2-N effectively mitigates plateau fading, it still suffers from capacity decay. In contrast, T2-BiN shows the best retention in both the plateau and overall capacity, indicating superior structural and interfacial stability. Fig. 4a and b depict the evolution of the oxidation and reduction peaks during cycling at 0.1 A g^{-1}. Initially, the sodium nucleation potentials for T2 and T2-N appear at 0.040 V and 0.043 V, respectively, whereas T2-BiN exhibits a higher value of 0.056 V, consistent with its enhanced nucleation kinetics. As cycling proceeds, the oxidation peaks of T2 and T2-N shift to lower voltages (0.011 V and 0.021 V), reflecting increased polarization. In contrast, T2-BiN shows only a slight shift to 0.048 V, indicating much more stable kinetics. A similar trend is observed in the reduction peaks, where the peak voltages increase from 0.096 V to 0.119 V for T2, from 0.095 V to 0.117 V for T2-N, and from 0.093 V to only 0.104 V for T2-BiN, highlighting its suppressed polarization. Sodium-ion diffusion behaviour was further investigated via the galvanostatic intermittent titration technique (GITT, Fig. 4c), and the corresponding diffusion coefficients (D_{Na^+}) were calculated (Fig. 4d).[47] All three anodes exhibit a similar trend, where the drop in D_{Na^+} from 0.1 V corresponds to the onset of Na^+ nucleation and pore-filling. For T2-BiN, a fluctuation in D_{Na^+} is observed between 0.5 and 0.3 V during the first discharge, attributed to the sodiation of Bi. Compared to T2, T2-N shows a significantly higher D_{Na^+}, owing to the presence of a Na_3N-rich SEI. More importantly, T2-BiN consistently exhibits the highest diffusion coefficients throughout subsequent cycling, which can be attributed to the formation of a thin SEI enriched with both Na_3N and NaF, as well as enhanced nucleation kinetics promoted by the diffused Bi.

The sodium storage behaviour of hard carbon was also studied by in situ Raman spectroscopy. The contour maps are given in Fig. 4e and f with the corresponding spectra shown in Fig. S19. For pristine T2, the D and G bands remain basically unchanged throughout the charge–discharge process. A slight decrease in D-band intensity during the middle stage is likely caused by Na^+ adsorption at edge defects. In contrast, T2-BiN exhibits noticeable spectral evolution. Shortly after the onset of discharge, the G-band shows a clear redshift, indicating the elongation of C–C bonds caused by Na^+ intercalation-induced stress.[6,48] It indicates the improved intercalation kinetics in T2-BiN driven by the expanded interlayer spacing and enhanced ion diffusion dynamics. Additionally, the intensity of the D-band significantly decreases along with the shift of the G band, suggesting increased Na^+ adsorption at defect sites. This likely results from the improved kinetics that enable Na^+ to access more interlayers and pores. Electrochemical impedance spectroscopy (EIS) was performed on T2, T2-N, and T2-BiN electrodes (Fig. S20) to investigate the impedance properties.
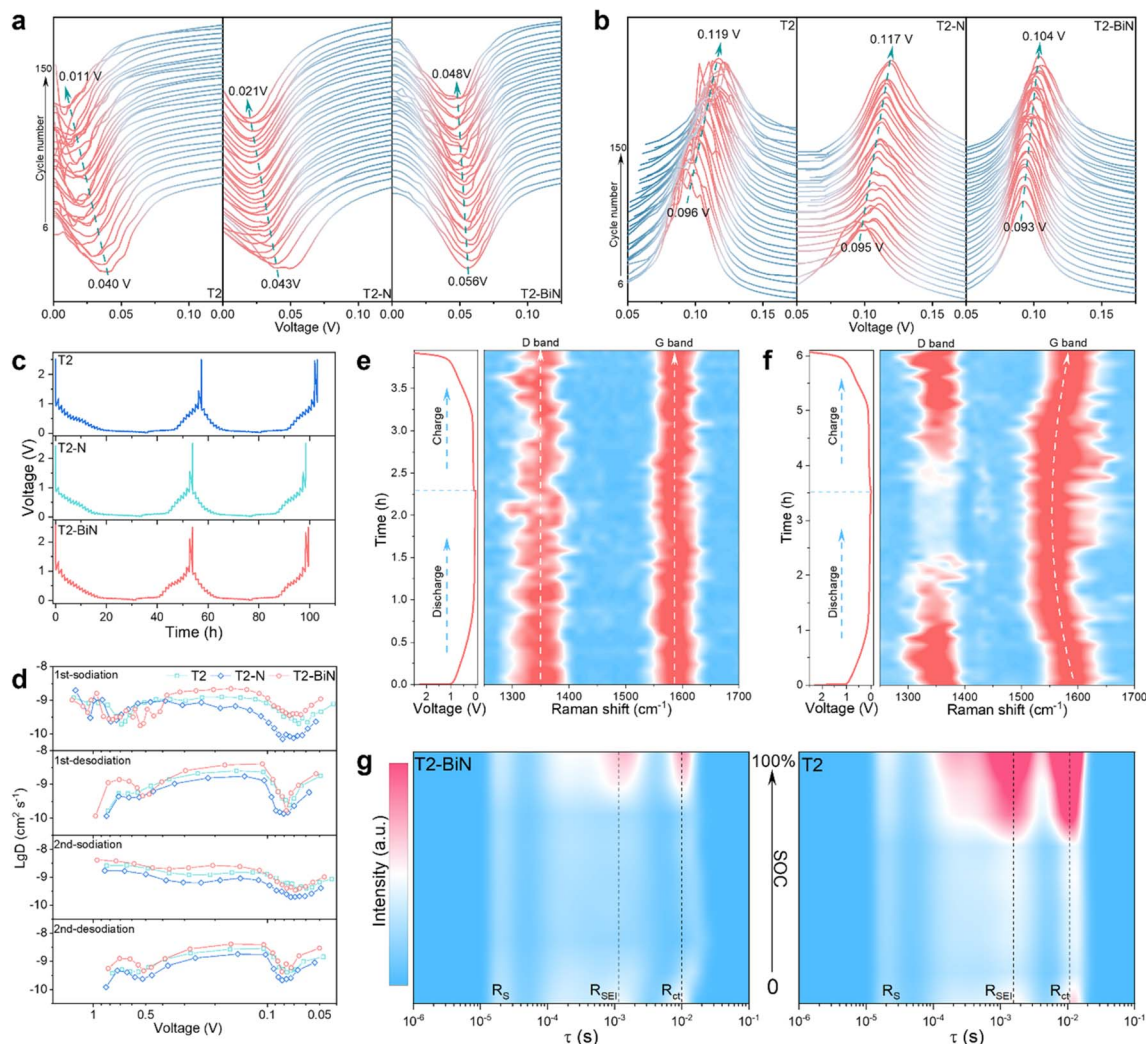
Fig. 4 Reaction kinetics and sodium-storage mechanism of T2 and T2-BiN. (a) The dQ/dV profiles showing the dynamic evolution of the reduction peak (a) and oxidation peak (b) during the cycling tests; (c) GITT profiles of the first two cycles and (d) the corresponding Na$^+$ diffusion coefficients; *in situ* Raman of T2 (e) and T2-BiN (f) showing the evolution of D and G band; (g) 2D DRT profiles of T2 and T2-BiN anodes during the first discharging process.

R_{ct} and the Warburg factor (σ) were fitted from the equivalent circuit model (inset in Fig. S20a) and the slopes of Z' *versus* $\omega^{-1/2}$ (Fig. S20b), respectively. Both of them were significantly reduced in T2-N and T2-BiN, indicating their good kinetics. *Operando* EIS measurements (Fig. S21) were conducted and interpreted *via* the distribution of relaxation time (DRT, Fig. S22) to further clarify the influence of SEI formation on interfacial kinetics. The DRT spectra reveal the SEI diffusion process in the relaxation time range of 10^{-3} to 10^{-4} s and the charge transfer process around 10^{-2} s.[49] The 2D DRT contour maps (Fig. 4g) clearly show that T2-BiN exhibits much lower SEI resistance (R_{SEI}) and charge transfer resistance (R_{ct}). More importantly, the relaxation times associated with R_{SEI} and R_{ct} are smaller than those of T2, suggesting faster processes in T2-BiN. This result clearly demonstrates that the superior ion diffusion and reaction kinetics of T2-BiN are directly related to its SEI characteristics.

SEI characterization

The SEI composition and structure was investigated in detail to elucidate the mechanism behind the excellent reaction kinetics and electrochemical performance. Cycled T2 and T2-BiN anodes were sliced to examine the element distribution on the cross-section of hard carbon particles (Fig. 5a, b and S23). Na and F were evenly coated on the surface of T2-BiN, with other elements uniformly distributed throughout the particles, indicating the formation of a homogeneous NaF-rich SEI. In contrast, the pristine T2 electrode exhibited low intensity and irregular distributions of Na and F, suggesting an uneven SEI and insufficient NaF content. Elemental line scans (Fig. S24) further confirmed these compositional differences between the two electrodes. 3D Modulus mapping (Fig. 5c) from AFM measurements demonstrated more uniform and higher mechanical strength on T2-BiN (average ~1.15 GPa) than on T2 (~0.71 GPa). This improvement can be attributed to its high
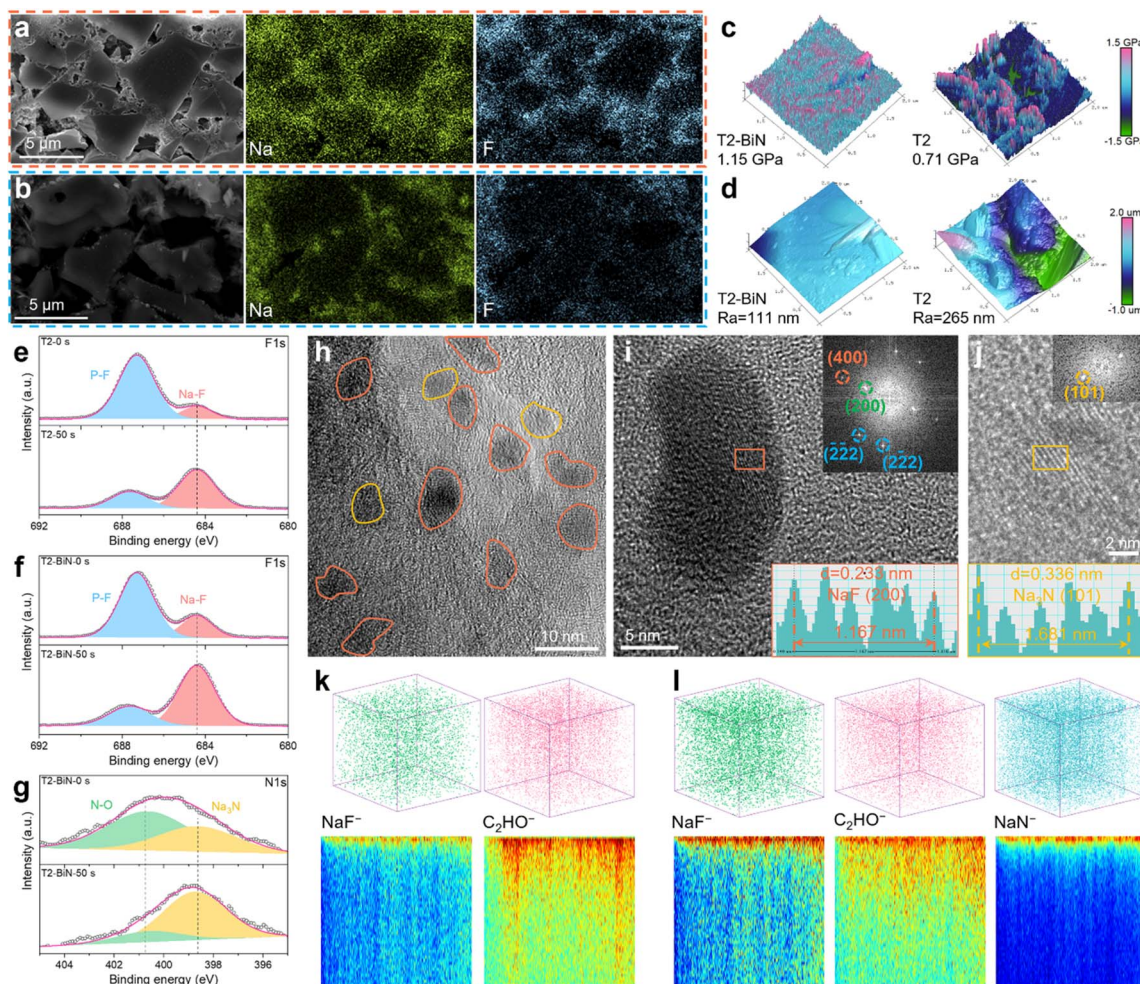
Fig. 5 Characterization of the SEI structures. Cross-sectional SEM and the corresponding mapping images of the cross-sections for cycled T2-BiN (a) and T2 (b) anodes; 3D modulus (c) and roughness (d) of the SEI on cycled T2 and T2-BiN anodes measured *via* AFM tapping mode; depth-profiling XPS F 1s spectra of cycled T2 (e) and T2-BiN (f) anodes; (g) depth-profiling XPS N 1s spectra of cycled T2-BiN anode; (h) TEM image showing the surface of cycled T2-BiN and the enlarged TEM images showing the crystal patterns of NaF (i) and Na₃N (j); TOF-SIMS 3D reconstruction distribution maps and cross projection of NaF⁻, C₂HO⁻ and NaN⁻ on cycled T2 (k) andT2-BiN (l) anodes.

content of mechanically robust NaF. Roughness mapping (Fig. 5d) showed that T2-BiN had a much smoother surface with a roughness (R_a) of 111 nm, compared to 265 nm for T2. This can be explained by the homogeneous and compact SEI that suppresses the electrolyte decomposition. In-depth XPS analysis was conducted to reveal the compositional variations in the SEI layers. Although the spectra show similar peaks, the intensity of C 1s and O 1s indicates more organic components on the surface of T2 and T2-N surface (Fig. S25 and S26). The carbon atomic ratios are 43.9% for T2, 37.6% for T2-N and only 27.2% for T2-BiN. Besides, T2-BiN showed significantly higher NaF content (Fig. 5e and f). Distinct Na_3N signals were observed in the N 1s spectra of both T2-N and T2-BiN (Fig. S26c and 5g). This results not only support the successful SEI modulation *via* the co-introduction of N and Bi, but also evidence the limited effect of N incorporation alone on the SEI content.

Cryo-TEM and HRTEM further visualized SEI morphology and composition. T2-BiN exhibited a uniform and thin SEI layer of ~25.6 nm thickness, compared to a thicker and irregular SEI

in the range of 31.1–48.7 nm on T2 (Fig. S27). The enlarged section (Fig. 5h) shows the presence of homogeneously distributed NaF and Na_3N on the surface of T2-BiN. The inter-planar spacing of 0.233 nm is in agreement with the (200) planes of NaF (Fig. 5i), while the interlayer spacing of 0.336 nm results from Na_3N (101) planes (Fig. 5j). TOF-SIMS mapping was employed to visualized the spatial distribution of various SEI species. Fig. 5k, l and S28 show that the distribution of NaF⁻ was more abundant and homogeneous on the surface of T2-BiN, whereas organic components like C_2HO^- penetrated deeper into T2. NaN⁻ signals were also mainly located at the outermost surface in T2-BiN. Their intensity changes are also clearly shown in the depth profiles (Fig. S29), supporting the enrichment of NaF and Na_3N inorganics in the SEI of T2-BiN. Besides, other NaF-related species (F⁻ and NaF_2^-) and the C⁻ species in Fig. S30 and S31 further evidence the NaF-less and thick SEI on the T2 surface. These results are consistent with the XPS and TEM results, emphasizing the formation of a thin, dense, uniform and NaF/Na_3N-riched SEI on T2-BiN. Such well-

tailored SEI characteristics were undoubtedly the reason for the well-improved sodium-storage kinetics and performance. The NaF/Na$_3$N-rich SEI integrates the mechanical robustness of NaF with the high ionic conductivity of Na$_3$N. Moreover, NaF forms a dense and stable passivation layer that suppresses electrolyte decomposition, maintaining a thin SEI, thereby maximizing the contribution of Na$_3$N to Na$^+$ transfer. This complementary functionality enhances both the structural integrity and ion-migration kinetics at the electrode/electrolyte interface, collectively contributing to the superior sodium storage performance of the T2-BiN electrode. These results also solidly verified the effectiveness of the interfacial chemistry regulation strategy, paving the way for the future development and practical application of hard carbon-based anodes.

Conclusions

In conclusion, we propose an interfacial chemistry regulation strategy to address the sluggish interfacial kinetics and limited nucleation efficiency of hard carbon anodes in ester-based sodium-ion batteries. Through a post-treatment approach using ammonium bismuth citrate as the precursor, both nitrogen and bismuth were successfully introduced, with Bi diffusing into the internal pores, as confirmed by EDS mapping and XPS analysis. Surface-deposited Bi effectively modulated the interfacial chemistry by eliminating the anion-depletion layer, thereby facilitating the formation of a thin, compact, and homogeneous NaF-rich SEI. Concurrently, nitrogen species were *in situ* converted into highly ion-conductive Na$_3$N, enabling an accelerated Na$^+$ diffusion rate. Additionally, the Bi species diffused into the pore interiors expanded the carbon interlayer and enhanced sodiophilicity, significantly lowering the barriers for Na$^+$ diffusion and nucleation. This dual-regulation of SEI and internal pore surfaces synergistically enhanced the sodium storage kinetics, resulting in exceptional rate performance (185.6 mA h g^{-1} at 0.5 A g^{-1}) and long-term cycling stability (84.4% capacity retention after 400 cycles). The assembled full cell exhibited a practical energy density of 237.2 W h kg^{-1} with almost no capacity decay for over 400 cycles at 2C. This work not only provides new insights into surface modulation in hard carbon but also offers a generalizable and scalable strategy to advance hard carbon anodes toward commercial applications.

Author contributions

L. L.: investigation, validation, data curation. J. Z.: conceptualization, methodology, and supervision. G. C. and Z. W.: validation, data curation, and visualization. L. W., and C. G.: data curation, and visualization. Y. C. conceptualization, methodology, supervision, and writing – original draft. X. C.: supervision, project administration and resources. C. W.: supervision.

Conflicts of interest

There are no conflicts to declare.

Data availability

The data supporting this article have been included as part of the SI.

Supplementary information: additional information about experimental and computational details, SEM EDS and cryo-TEM images, Raman, SAXS and XPS spectra, more electrochemical and TOF-SIMS results. See DOI: https://doi.org/10.1039/d5sc04111b.

Acknowledgements

Notes and references

1 M. Yang, Q. Chen, Q. Wen, L. Li, C. Wu, X. Wu and S. Chou, *Sci. China: Chem.*, 2025, **68**, DOI: 10.1007/s11426-025-2602-9.

2 Y. Li, A. Vasileiadis, Q. Zhou, Y. Lu, Q. Meng, Y. Li, P. Ombrini, J. Zhao, Z. Chen, Y. Niu, X. Qi, F. Xie, R. van der Jagt, S. Ganapathy, M.-M. Titirici, H. Li, L. Chen, M. Wagemaker and Y.-S. Hu, *Nat. Energy*, 2024, **9**, 134–142.

3 F. Cheng, J. Hu, W. Zhang, B. Guo, P. Yu, X. Sun and J. Peng, *Energy Environ. Sci.*, 2025, **18**, 6874–6898.

4 X. Feng, Y. Li, Y. Li, M. Liu, L. Zheng, Y. Gong, R. Zhang, F. Wu, C. Wu and Y. Bai, *Energy Environ. Sci.*, 2024, **17**, 1387–1396.

5 Y. Zhang, S. W. Zhang, Y. Chu, J. Zhang, H. Xue, Y. Jia, T. Cao, D. Qiu, X. Zou, D. W. Wang, Y. Tao, G. Zhong, Z. Peng, F. Kang, W. Lv and Q. H. Yang, *Nat. Commun.*, 2025, **16**, 3634.

6 C. Wu, Y. Yang, Y. Li, X. He, Y. Zhang, W. Huang, Q. Chen, X. Liu, S. Chen, Q. Gu, L. Li, S. C. Smith, X. Tan, Y. Yu, X. Wu and S. Chou, *Energy Environ. Sci.*, 2025, **18**, 6019–6031.

7 M. Liu, F. Wu, Y. Gong, Y. Li, Y. Li, X. Feng, Q. Li, C. Wu and Y. Bai, *Adv. Mater.*, 2023, **35**(29), 2300002.

8 Y. Sun, D. Zuo, C. Xu, B. Peng, J.-C. Li, J. Yang, S. Xu, X. Sun, H. Zhou and S. Guo, *Energy Environ. Sci.*, 2025, **18**, 1911–1919.

9 F. Li, K. Ren, M. Hou, M. Lin, X. Yang, Y. Zhou, S. Xiong and F. Liang, *ACS Energy Lett.*, 2025, **10**, 195–204.

10 J. Sun, Y. Li, L. Lv, L. Wang, W. Xiong, L. Huang, Q. Qu, Y. Wang, M. Shen and H. Zheng, *Adv. Funct. Mater.*, 2024, **34**(52), 2410693.

11 Y. Dong, Y. Chen, X. Yue and Z. Liang, *Energy Environ. Sci.*, 2024, **17**, 2500–2511.

12 L. Wang, J. Guo, Q. Qi, X. Li, Y. Ge, H. Li, Y. Chao, J. Du and X. Cui, *Nano-Micro Lett.*, 2025, **17**, 111.

13 S. Wan, K. Song, J. Chen, S. Zhao, W. Ma, W. Chen and S. Chen, *J. Am. Chem. Soc.*, 2023, **145**, 21661–21671.

14 W. Tian, G. Lin, S. Yuan, T. Jin, Q. Wang and L. Jiao, *Angew. Chem., Int. Ed.*, 2025, **64**, e202423075.

15 C. Hu, S. Guo, F. Huang, Y. Yang, C. Yan, C. Z. Zhao, S. Liang, G. Fang and Q. Zhang, *Angew. Chem., Int. Ed.*, 2024, **63**, e202407075.

16 S. Zhao and F. Huang, *ACS Nano*, 2024, **18**, 1733–1743.

17 G. Zhang, C. Fu, S. Gao, H. Zhao, C. Ma, Z. Liu, S. Li, Z. Ju, H. Huo, P. Zuo, G. Yin, T. Liu and Y. Ma, *Angew. Chem., Int. Ed.*, 2024, **64**(15), e202424028.

18 M. Liu, Z. Jiang, X. Wu, F. Liu, W. Li, D. Meng, A. Wei, P. Nie, W. Zhang and W. Zheng, *Angew. Chem., Int. Ed.*, 2024, **64**(17), e202425507.

19 L. Chen, M. Chen, Q. Meng, J. Zhang, G. Feng, X. Ai, Y. Cao and Z. Chen, *Angew. Chem., Int. Ed.*, 2024, **63**, e202407717.

20 G. Chen, J. Zhu, T. Li, L. Liu, J. Zou, Z. Wang, Y. Chao, X. Cui and W. Chen, *Energy Storage Mater.*, 2025, **79**, 104349.

21 F. Wang, L. Chen, J. Wei, C. Diao, F. Li, C. Du, Z. Bai, Y. Zhang, O. I. Malyi, X. Chen, Y. Tang and X. Bao, *Energy Environ. Sci.*, 2025, **18**, 4312–4323.

22 S. Hou, D. Zhang, Y. Lei, Y. Zhou, D. Yang, P. Dong, B. Xu, B. Yang and F. Liang, *Langmuir*, 2025, **41**(6), 4259–4269.

23 H. Zhang, S. Lin, C. Shu, Z. Tang, X. Wang, Y. Wu and W. Tang, *Mater. Today*, 2025, **85**, 231–252.

24 C. Chen, Y. Tian, R. Ren, S. Duan, D. Wang, Z. Wang, Y. Chao, J. Zhu and X. Cui, *Adv. Sci.*, 2025, 2510328.

25 J. C. Hyun, H. M. Jin, J. H. Kwak, S. Ha, D. H. Kang, H. S. Kim, S. Kim, M. Park, C. Y. Kim, J. Yoon, J. S. Park, J. Y. Kim, H. D. Lim, S. Y. Cho, H. J. Jin and Y. S. Yun, *Energy Environ. Sci.*, 2024, **17**, 2856–2863.

26 S. Xiao, Y.-J. Guo, H.-X. Chen, H. Liu, Z.-Q. Lei, L.-B. Huang, R.-X. Jin, X.-C. Su, Q. Zhang and Y.-G. Guo, *Adv. Mater.*, 2025, **37**, 28.

27 T. Jin, X. Y. Zhang, S. Yuan and L. Yu, *Sci. Adv.*, 2025, **11**, 6483.

28 N. LeGe, Y. H. Zhang, W. H. Lai, X. X. He, Y. X. Wang, L. F. Zhao, M. Liu, X. Wu and S. L. Chou, *Chem. Sci.*, 2024, **16**, 1179–1188.

29 D. Qiu, W. Zhao, B. Zhang, M. T. Ahsan, Y. Wang, L. Zhang, X. Yang and Y. Hou, *Adv. Energy Mater.*, 2024, **14**(20), 2400002.

30 C. Wu, W. Huang, Y. Zhang, Q. Chen, L. Li, Y. Zhang, X. Wu and S. L. Chou, *eScience*, 2025, **5**, 100371.

31 D. X. Han and P. J. Sun, *Energy Storage Mater.*, 2023, **58**, 344–352.

32 J. Luo, K. Yang, J. Gai, X. Zhang, C. Peng, C. Qin, Y. Ding, Y. Yuan, Z. Xie, P. Yan, Y. Cao, J. Lu and W. Chen, *Angew. Chem., Int. Ed.*, 2024, **64**(7), e202419490.

33 R. Zhang, T. Shui, A. Li, H. Xia, G. Xu, L. Ji, C. Lu, W. Zhang and Z. M. Sun, *Energy Environ. Sci.*, 2025, **18**, 1011–1026.

34 J. Zhao, X. X. He, W. H. Lai, Z. Yang, X. H. Liu, L. Li, Y. Qiao, Y. Xiao, L. Li, X. Wu and S. L. Chou, *Adv. Energy Mater.*, 2023, **13**(18), 2300444.

35 X. Wei, Y. Yi, X. Yuan, Y. Liu, Q. Wan, G. Gou, Y. Zhang, G. Zhou and Y. Song, *Energy Environ. Sci.*, 2024, **17**, 2968–3003.

36 N. LeGe, Y. H. Zhang, W. H. Lai, X. X. He, Y. X. Wang, L. F. Zhao, M. Liu, X. Wu and S. L. Chou, *Chem. Sci.*, 2025, **16**, 1179–1188.

37 J. Cui, W. Li, P. Su, X. Song, W. Ye, Y. Zhang and Z. Chen, *Adv. Energy Mater.*, 2025, **15**(31), 2502082.

38 C. Yu, Y. Li, H. Ren, J. Qian, S. Wang, X. Feng, M. Liu, Y. Bai and C. Wu, *Carbon Energy*, 2022, **5**(1), e220.

39 Z.-G. Liu, J. Zhao, H. Yao, X.-X. He, H. Zhang, Y. Qiao, X.-Q. Wu, L. Li and S.-L. Chou, *Chem. Sci.*, 2024, **15**, 8478–8487.

40 Z. Fang, S. Fan, Z. Yan, D. Tang, X. Gao, X. Huang, H. Zheng, B. Wang, Q. Jiang, J. Han, J. Lin, Q. Xie, D. L. Peng and Q. Wei, *Adv. Mater.*, 2024, **37**(3), 2412636.

41 P. Zheng, W. Zhou, Y. Mo, B. Zheng, M. Han, Q. Zhong, W. Yang, P. Gao, L. Yang and J. Liu, *J. Energy Chem.*, 2025, **100**, 730–738.

42 Y. Wang, Z. Yi, L. Xie, Y. Mao, W. Ji, Z. Liu, X. Wei, F. Su and C. M. Chen, *Adv. Mater.*, 2024, **36**(26), 2401249.

43 C. Qiu, A. Li, D. Qiu, Y. Wu, Z. Jiang, J. Zhang, J. Xiao, R. Yuan, Z. Jiang, X. Liu, X. Chen and H. Song, *ACS Nano*, 2024, **18**, 11941–11954.

44 Z. Fu, D. Jiang, Z. Tang, Z. Tang, J. Zhou, R. Liu, H. Li, D. Sun, Y. Tang and H. Wang, *Chem. Eng. J.*, 2025, **505**, 159431.

45 J. Zheng, Y. Wu, C. Guan, D. Wang, Y. Lai, J. Li, F. Yang, S. Li and Z. Zhang, *Carbon Energy*, 2024, **6**, e538.

46 W. Li, X. Guo, K. Song, J. Chen, J. Zhang, G. Tang, C. Liu, W. Chen and C. Shen, *Adv. Energy Mater.*, 2023, **13**(22), 2300648.

47 D. Wang, Y. Chao, K. Guo, Z. Wang, M. Yang, J. Zhu, X. Cui and Q. Xu, *Adv. Funct. Mater.*, 2024, **34**(40), 2405642.

48 H. Wang, Y. Chao, J. Li, Q. Qi, J. Lu, P. Yan, Y. Nie, L. Wang, J. Chen and X. Cui, *J. Am. Chem. Soc.*, 2024, **146**, 17041–17053.

49 J. Pan, Z. Sun, X. Wu, T. Liu, Y. Xing, J. Chen, Z. Xue, D. Tang, X. Dong, H. Zhang, H. Liu, Q. Wei, D. L. Peng, K. Amine and Q. Zhang, *J. Am. Chem. Soc.*, 2025, **147**, 3061.